

Article

Optimizing Discharge Capacity of Graphite Nanosheet Electrodes for Lithium–Oxygen Batteries

Philipp Wunderlich *, Jannis Küpper and Ulrich Simon

Institute of Inorganic Chemistry, RWTH Aachen University, 52072 Aachen, Germany;
jannis.kuepper@ac.rwth-aachen.de (J.K.); ulrich.simon@ac.rwth-aachen.de (U.S.)

* Correspondence: philipp.wunderlich@rwth-aachen.de; Tel.: +49-241-809-4644

Received: 25 May 2020; Accepted: 24 June 2020; Published: 1 July 2020



Abstract: Lithium–oxygen ($\text{Li}-\text{O}_2$) batteries require scalable air electrode concepts and a sensible choice of operation parameters to achieve their promised energy densities. Furthermore, different test parameters are often investigated individually, but rarely brought together in order to optimize the discharge process and unlock the full discharge capability of an air electrode. In this work, we present a highly porous electrode based on graphite nanosheets (GNS) and discuss the impact of the discharge current density and the oxygen pressure as battery test parameters, as well as the electrolyte salt and volume, on the discharge behavior. In particular, changing the electrolyte salt from LiNO_3 to LiTFSI proved to be an important step towards better cell performance, because synergistic effects of the electrolyte and GNS greatly enhance the carbon-specific capacity. The optimized combination of the aforementioned parameters enabled a remarkably high discharge capacity of 56.3 mAh/cm^2 ($5860 \text{ mAh/g}_{\text{carbon}}$) obtained at $150 \mu\text{A/cm}^2$ ($15.6 \text{ mA/g}_{\text{carbon}}$), resulting in the almost complete conversion of the lithium anode. These experimental results are an important step towards practical high-capacity air electrodes for $\text{Li}-\text{O}_2$ batteries.

Keywords: lithium–oxygen batteries; air electrode; high-capacity; nanographite; electrolyte

1. Introduction

The lithium–oxygen ($\text{Li}-\text{O}_2$) battery has the potential of storing a higher amount of energy at lower cost than present-day lithium-ion batteries, which makes this challenging cell chemistry appealing for portable energy storage systems [1]. $\text{Li}-\text{O}_2$ cells comprise lithium metal anodes and oxygen as cathode reactant, which, in the main discharge reaction, are converted into lithium peroxide [2]:



The discharge mechanism proceeds through the following steps: (i) O_2 adsorption on the electrode surface, (ii) O_2 reduction to a superoxide anion (ORR), (iii) combination with Li^+ forming LiO_2 , (iv) transformation into Li_2O_2 by disproportionation or a second electron transfer step [3]. The intermediate LiO_2 can be stabilized in solution, shifting the mechanism from Li_2O_2 thin film growth via a surface-bound route to precipitation and growth of particles via a solution-stabilized route [4,5]. Parameters that can influence the reaction kinetics are the current density (j), the oxygen pressure (p_{O_2}) and the choice of electrolyte [3]. Two of the most commonly used electrolyte salts are lithium nitrate (LiNO_3) and lithium bis(trifluoromethanesulfonyl)imide (LiTFSI) in combination with an ether as solvent [4,6]. LiNO_3 is low-cost, non-toxic, helps to stabilize the lithium anode, and due to its high donor number (22 kcal/mol), it supports the solution-based precipitation of Li_2O_2 particles. LiTFSI has the highest Li^+ conductivity and can be considered as highly dissociated salt. With its

donor number of 11 kcal/mol, it is known for significantly supporting the surface-based deposition of Li_2O_2 thin films [5–7].

Besides the fundamental challenges of $\text{Li}-\text{O}_2$ electrochemistry, there are practical challenges that must also be addressed to keep the promises of a low-cost, high-energy battery. It was estimated that rechargeable $\text{Li}-\text{O}_2$ batteries possess an estimated practical specific energy of up to 1000 Wh/kg [8,9], but in order to meet these goals, $\text{Li}-\text{O}_2$ cells must be capable of reaching high discharge capacities with little overpotential losses. At the same time, batteries must be able to cycle at high depths of discharge. These challenges can partially be addressed by an efficient air electrode design [10,11]. One goal for high-capacity air electrodes is to provide pore space for as many discharge reaction products as possible with the lowest possible electrode mass. Benchmarking cathode materials is generally based on their mass-specific capacities (mAh/g), which has been exploited by making electrodes lighter (<1 mg), instead of designing them for a large discharge product uptake and a high degree of conversion of the lithium anode. Additionally, capacities are often referred to as electrode or even catalyst weights only, disregarding the combined mass of any additional substrates and binders [12]. The same holds true for current densities or capacitive cycling limits, which are commonly referred to as the aforementioned low “active” mass as well, which artificially pushes the rate performance or the cycle numbers to unrealistically high values, thus creating the need for more transparent reporting standards [13]. The practical usefulness of air electrodes is better benchmarked by the areal capacity (mAh/cm²) [13]. In the following, a selection of more practical high-capacity electrodes for $\text{Li}-\text{O}_2$ batteries is presented: carbon nanotubes (CNT) in between gas diffusion layers (30 mAh/cm²) [14], dry-pressed holey graphene (41.1 mAh/cm²) [15], CNT/Ketjen black electrode stacks (38.9 mAh/cm²) [16] and a CNT-monolith electrode (102.5 mAh/cm²) [17]. To our knowledge, the latter is the highest areal capacity ever reported for a $\text{Li}-\text{O}_2$ battery.

In this work, we optimize the discharge capacity of cells comprising an air electrode based on nanographite-loaded polymer foams (GNS-foams) [18]. The graphite nanosheets (GNS) show an anomalous discharge behavior that we attribute to the activation of individual graphene layers, which enable electrochemical reactions beyond the saturation of the outer particle surface [18]. We further elucidate and harness this mechanism by carrying out battery tests with an altered set of parameters: the current density, the oxygen pressure, the electrolyte salt and volume. In an attempt to reach the maximum cell capacity, which is given by the full faradaic conversion of the lithium anode, we optimize a combination of cell test parameters and scale up the electrode for a high-capacity discharge experiment. The analysis of the discharge products is carried out with scanning electron microscopy (SEM), energy-dispersive X-ray spectroscopy (EDS), Raman spectroscopy and powder X-ray diffraction (XRD).

2. Materials and Methods

The assembly of $\text{Li}-\text{O}_2$ cells and preparation of GNS-loaded foam electrodes were performed as described in our previous work [18].

In brief, gas diffusion electrodes were prepared by loading an Au-coated melamine foam disc with 40 mg GNS (Strem Chemicals, Inc., Newburyport, MA, USA) via dip-coating with isopropanol. The typical cathode mass was 15 mg, of which 10 mg is the GNS (carbon) mass. “ECC-Air” test cells (EL-Cell GmbH, Hamburg Germany) were assembled using lithium discs (Rockwood, Frankfurt am Main, Germany) with a mass of 40 mg, ceramic-coated polymer sheets as separators (Freudenberg, Weinheim, Germany), and GNS-foams as cathodes. The disc diameters were 18 mm for the electrodes and 20 mm for the separator. All materials, including the salts, were dried overnight at 100 °C and solvents were dried over 4 Å molecular sieves for at least one week. The cell assembly process was carried out in an Ar-filled glovebox. The two electrolyte solutions featured in this work were 1.0 M LiTFSI (99.95%, Sigma Aldrich, Steinheim, Germany) and 0.5 M LiNO₃ (battery grade 99.999%, Alfa Aesar, Karlsruhe, Germany) in tetraethylene glycol dimethyl ether (TEGDME, >99%, Sigma-Aldrich, Steinheim, Germany). Typically, 200 µL of electrolyte was used in each

cell. Fully assembled batteries were transported to the test bench and connected to the O₂ supply. After thorough purging they could equilibrate for at least 6 h prior to testing. Unless otherwise stated, the O₂ pressure was 4 atm. Galvanostatic discharge experiments were performed at a rate of 150 $\mu\text{A}/\text{cm}^2$ using a Basytec CTS Lab battery tester (Basytec, Asselfingen, Germany). All current densities were referred to as the geometrical surface area of both the anode and cathode, which is 2.54 cm^2 . All cell voltages were referred to as the potential of Li/Li⁺, and the discharge tests were terminated when a cell dropped below 2.0 V.

The water contents of both electrolyte solutions were obtained from Karl Fischer titration (831 KF coulometer from Metrohm, Herisau, Switzerland). The respective electrical conductivities were determined using a conductivity meter (LAB 945 from SI Analytics, Germany) in combination with a conductivity measuring cell with a cell constant of 1.0 $\mu\text{S}\cdot\text{cm}^{-1}$ (ScienceLine LF 713 T from SI Analytics, Mainz, Germany). For the conductivity measurements, electrolyte solutions were prepared in an Ar-filled glovebox and transferred to a climatic chamber (MK 53 from Binder, Tuttlingen, Germany) without air exposure. The temperature inside the chamber was set to 25.0 °C and measurements were performed after an equilibration period of at least 15 min.

Cathode samples to be characterized post mortem were rinsed with 1,2-dimethoxyethane (>99.5%, Sigma-Aldrich, Steinheim, Germany) in order to remove residual electrolyte. Dried samples were analyzed by means of SEM (LEO Supra 35VP from Carl Zeiss AG, Oberkochen, Germany) in combination with EDS (INCA Energy 200 detector from Oxford Instruments, Abingdon, UK), Raman spectroscopy (LabRAM 300 from Horiba, Kyoto, Japan), and XRD (StadiP powder diffractometer by Stoe&Cie, Darmstadt, Germany). A detailed description of the measurement setup and methodology for these techniques can be found in our previously published work [18].

3. Results and Discussion

3.1. Rate Capability

The current density dependence of the discharge capacity is known to be particularly pronounced in Li-O₂ batteries, because the current directly affects the growth of the discharge products [3,19,20]. Here, we alter the discharge current in order to investigate how it affects the discharge capacity of our GNS-based electrodes, which previously showed an unusual two-step discharge behavior [18]. The rate performance of GNS-based batteries is tested up to one order of magnitude above and below the standard current density of 150 $\mu\text{A}/\text{cm}^2$ (Figure 1).

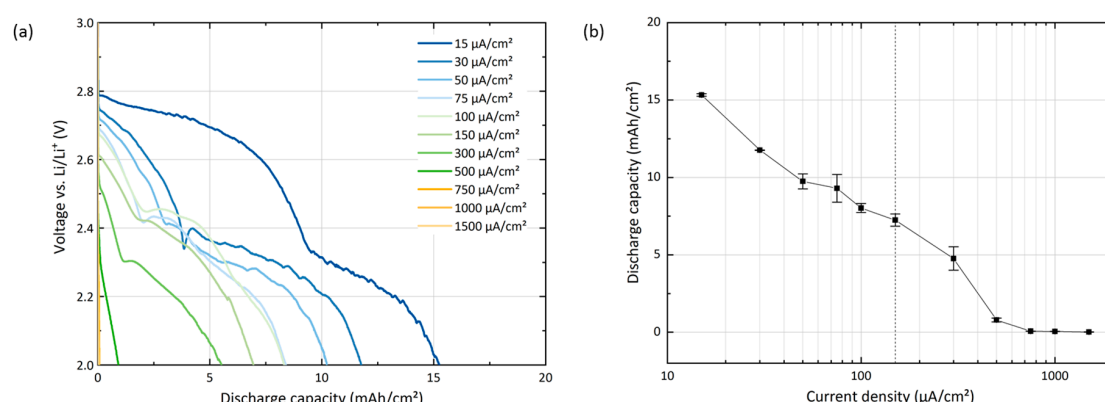


Figure 1. Discharge data for GNS-foam electrodes with current densities between 15 $\mu\text{A}/\text{cm}^2$ and 1.5 mA/cm². (a) $U(Q)$ profiles. (b) $Q(j)$ plot with the data of three cells for each current density. The dashed line indicates the standard rate of 150 $\mu\text{A}/\text{cm}^2$. A logarithmic and a normalized representation of the data, with better visibility of the discharge curves at high current densities, can be found in the supporting information (Figure S1).

Experiments performed at the standard rate of $150 \mu\text{A}/\text{cm}^2$ give a reproducible discharge capacity of $7.2 \text{ mAh}/\text{cm}^2 \pm 0.4 \text{ mAh}/\text{cm}^2$. Increasing or decreasing the rate by one order of magnitude has a significant effect on the discharge capacity: the slowest rate of $15 \mu\text{A}/\text{cm}^2$ results in more than double the capacity ($15.3 \text{ mAh}/\text{cm}^2 \pm 0.1 \text{ mAh}/\text{cm}^2$) compared to the standard rate and a greatly decreased overpotential. However, these positive effects need to be carefully weighed against the low power density and the extended test duration of 42 days. The highest rate of $1.5 \text{ mA}/\text{cm}^2$ results in a negligible discharge capacity of only $0.016 \text{ mAh}/\text{cm}^2 \pm 0.012 \text{ mAh}/\text{cm}^2$ and a test duration of only a few minutes. The current density dependence of the capacity is illustrated in Figure 1b. At low current densities, the capacity falls exponentially with increasing current density. In the range between $300 \mu\text{A}/\text{cm}^2$ and $500 \mu\text{A}/\text{cm}^2$, it falls even more rapidly.

The most distinct feature of the discharge curves of GNS-electrodes is the two-stage profile with a slope change at about $2.4 \text{ V} \pm 0.1 \text{ V}$. Based on our in-depth study on this discharge profile [18], the deep discharge of GNS-foam electrodes can be divided into stage I and stage II: the first stage represents the “typical” Li-O₂ behavior, in which discharge products are being deposited on the surface of the cathode particles. The second stage is related to the layered structure of the graphite particles, which undergoes severe volume expansion and allows for further faradaic reactions [18]. In this rate capability test, the anomalous behavior shows up for all cells that are discharged at current densities between $15 \mu\text{A}/\text{cm}^2$ and $500 \mu\text{A}/\text{cm}^2$, which can be seen more clearly in the logarithmic representation of the discharge profile plot in Figure S1a. The normalized discharge profiles in Figure S1b show the voltage curve in dependence of the depth of discharge (DoD). When lowering the current density, the onset of the stage II is delayed from about 25% DoD at $150 \mu\text{A}/\text{cm}^2$ to 60% DoD at $15 \mu\text{A}/\text{cm}^2$. The share of desired discharge behavior (stage I) can thus effectively be increased by lowering the discharge rate. In some cases, the transition between the two discharge stages is accompanied by a voltage dip, which is best seen in the test at $30 \mu\text{A}/\text{cm}^2$. This phenomenon (also known as coup de fouet) is likely caused by the super-saturation of the electrolyte with reaction intermediates (e.g., LiO₂) and their subsequent nucleation after overcoming a nucleation overpotential [21–23]. Stage II discharge is not initiated for current densities $\geq 750 \mu\text{A}/\text{cm}^2$ and the discharge capacity drastically drops to values below $0.08 \text{ mAh}/\text{cm}^2$. Increasing the current directly increases the IR polarization of the cell, which shifts the onset potential of stage II below the cut-off at 2.0 V and thus ends the test after stage I. The two-stage mechanism is strongly current-density-dependent, which may be the reason that it has not been observed in other graphite-based electrodes, simply because the discharge currents were too high (or the amount of graphite was too small).

In addition to the electrochemical data, the electrode samples are analyzed post mortem via SEM to investigate the GNS surface after discharge. Prior experimental studies have already investigated the growth mechanisms of the discharge products [19,20,24]. However, we want to check whether the models are also applicable to GNS electrodes and gain more detailed insights into what may cause the end of discharge.

The SEM images in Figure 2 illustrate how the discharge product morphology changes, from rather thin film-like deposits on the GNS surface at $1.5 \text{ mA}/\text{cm}^2$ (b), to micrometer-sized toroidal particles at $15 \mu\text{A}/\text{cm}^2$ (f). The formation of Li₂O₂ toroids is caused by heterogeneous nucleation and growth as a function of current density, state of discharge, electrolyte properties and possibly by impurities such as H₂O [4]. Higher rates induce more nucleation that results in smaller particles resembling a thin film deposit. Low rates support the precipitation of Li₂O₂ from the solution on existing Li₂O₂ particles, and the deposits can thus grow in size without covering the carbon surface [19,20,24]. Grown onto GNS, the Li₂O₂ particle diameter decreases from the largest structures of up to $1.3 \mu\text{m}$ to less than 150 nm with increasing current density, following the measured capacity trend. Increasing the rate not only decreases the particle size, but also increases the particle number due to a higher nucleation rate [20]. The GNS surface after full discharge at $1.5 \text{ mA}/\text{cm}^2$ shows no particulate discharge products. GNS are covered in a thin layer, which is not necessarily Li₂O₂, but could also be residual electrolyte or a solid electrolyte interphase (SEI) layer.

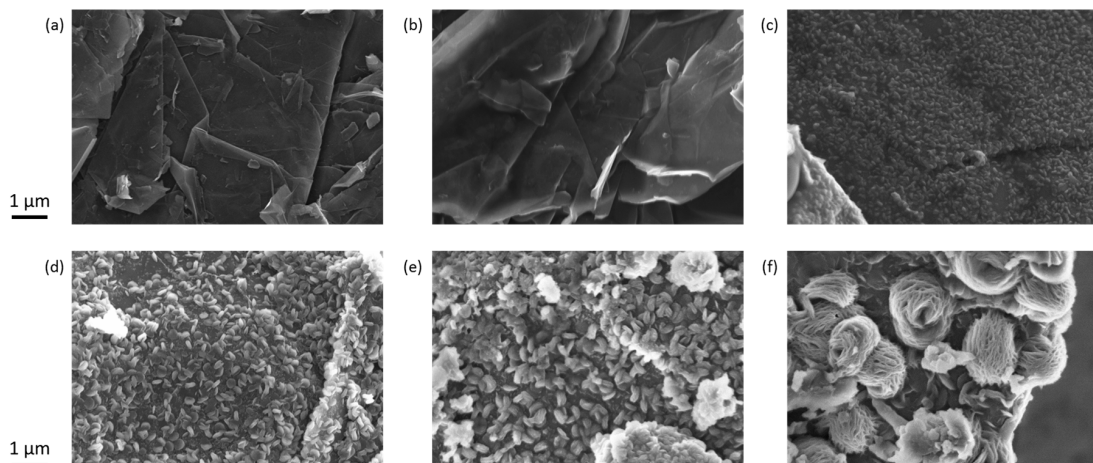


Figure 2. SEM images of discharge products on GNS obtained after full discharge at various rates. All images were taken from GNS at the electrode top (O_2 -rich side). (a) Pristine GNS for reference. Discharged GNS samples with current densities of (b) $1.5 \text{ mA}/\text{cm}^2$, (c) $500 \mu\text{A}/\text{cm}^2$, (d) $150 \mu\text{A}/\text{cm}^2$, (e) $50 \mu\text{A}/\text{cm}^2$ and (f) $15 \mu\text{A}/\text{cm}^2$. See Figure 1 for the respective discharge capacities.

The transition from particulate to thin film discharge products could be explained by transport limitations, which can cause a sharp capacity drop in the $Q(j)$ profile [25]. For the given system, this is observed in Figure 1b between $300 \mu\text{A}/\text{cm}^2$ and $500 \mu\text{A}/\text{cm}^2$. The loss of capacity can have several causes, which depend on the electrode–electrolyte system and is matter of discussion: (i) rate-limiting reaction steps like the ORR, (ii) O_2 transport or (iii) Li^+ transport limitation, (iv) high cell impedance and dielectric passivation can end the discharge [24,26–28]. Current densities of $500 \mu\text{A}/\text{cm}^2$ and higher result in fairly low amounts of deposited discharge products, which makes an end of discharge due to high cell impedance unlikely. [18]. The overpotential can be of kinetic origin, but the contribution of ohmic polarization plays a major role as well. Therefore, in order to increase the rate capability of the GNS electrodes, the cell impedance should be lowered.

Generally, a low discharge current density appears as the most effective parameter to both increase the capacity and lower the overpotential, but it may not be suitable when it comes to practical applications. The strong current-dependency of the discharge capacity will render it difficult for Li-O₂ cells to achieve their theoretical energy density even at moderate power demands. Generally, C-rates are rarely reported in Li-O₂ literature due to the limited reproducibility of cells. However, our system allows us to give an estimation: discharge at $150 \mu\text{A}/\text{cm}^2$ corresponds to C/45, which is a fairly small rate compared to Li-ion batteries that can handle 1C or more. For practical applications that demand more than $1 \text{ mA}/\text{cm}^2$, the Li-O₂ cell performance must be improved significantly. A higher power density (on the cell stack level) could be realized by using thinner electrodes with low tortuosity and shorter mass transport distances. The electrode porosity shall also be optimized by making it as small as necessary to host the discharge products, but avoid pore clogging at the same time. However, downscaled cathodes also imply that there will be more discharge product (mass) on less active material, which will cause a high cell impedances that in turn limits the discharge capacity. While the properties of the lithium anode are fixed and the electrolyte conductivity is physically limited, only cathode upscaling allows for more parallel reaction sites and, eventually, a better rate capability. In the following sections the current density is kept constant at $150 \mu\text{A}/\text{cm}^2$ in order to keep the test times in a reasonable duration of a few days.

3.2. Oxygen Pressure

The O_2 pressure is a parameter that is often overlooked, but should definitely be considered for high-performance Li-O₂ cells due to its known beneficial effects on the discharge capacity and rate capability, and also the O_2 solubility and diffusivity [29,30]. In most studies it is typically kept at (only)

1 atm over atmosphere, and higher values are rarely made use of and investigated, despite the fact that insufficient pressure can kinetically restrict the electrochemical reactions [31]. Therefore, we operate the Li–O₂ batteries at an elevated pressure of 4 atm. The effects of a varied oxygen pressure on the discharge behavior of GNS electrodes are depicted in Figure 3.

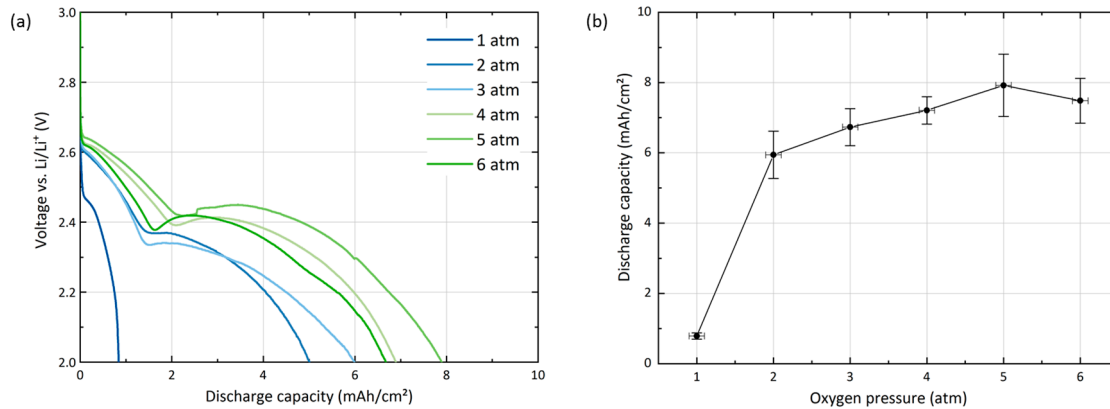


Figure 3. (a) $U(Q)$ profiles of GNS-loaded foam electrodes discharged at $150 \mu\text{A}/\text{cm}^2$ with oxygen pressures ranging from 1 atm (ambient pressure) to 6 atm. (b) $Q(p)$ plot with the discharge data of three cells tested at each pressure.

At ambient oxygen pressure (1 atm), a discharge capacity of only $0.8 \text{ mAh}/\text{cm}^2 \pm 0.1 \text{ mAh}/\text{cm}^2$ is reached and the cell does not exhibit the characteristic two-step profile of the GNS electrode. At 2 atm, the capacity reaches $5.9 \text{ mAh}/\text{cm}^2 \pm 0.7 \text{ mAh}/\text{cm}^2$, which is already close to the values for the cells at 4 atm ($7.2 \text{ mAh}/\text{cm}^2 \pm 0.4 \text{ mAh}/\text{cm}^2$). The largest capacity of $7.9 \text{ mAh}/\text{cm}^2 \pm 0.9 \text{ mAh}/\text{cm}^2$ is obtained at 5 atm. Increasing O₂ pressure even further does not result in higher capacities, as cells discharged at 6 atm reach $7.5 \text{ mAh}/\text{cm}^2 \pm 0.6 \text{ mAh}/\text{cm}^2$. Supplementary Information Figure S2 shows the discharge profile of an additional test that was carried out at 11 atm (cell-hardware limit) and does not show an improved performance. In contrast to the positive effects caused by a decrease in current density, the discharge voltages and overpotentials of the cells are not significantly affected by O₂ pressure. The observed differences in voltage levels for the tests with 3 atm or higher are within the standard deviation range for GNS electrodes [18].

The poor discharge capacity obtained at 1 atm demonstrates the performance-limiting effect of an O₂ pressure that is too low. It may be explained mechanistically by the O₂ availability for the ORR during discharge. The perpetual depletion of O₂ at the electrolyte–electrode interface is counteracted by a near-infinite O₂ supply from the gaseous phase, which is transported to the cathode surface through the electrolyte. The rate of O₂ replenishment by diffusion is determined by the overall O₂ concentration in the electrolyte and the rate of O₂ dissolution from the gas phase. Both are factors that strongly depend on the O₂ pressure [32]. If the O₂ availability at the electrolyte–electrode interface is not sufficient, higher overpotentials and lower discharge capacities are the consequences [29–31]. Furthermore, a lack of O₂ adsorption on the cathode surface may also lead to an early end of discharge or diminished reaction rates [31,33]. Higher pressures generally promote O₂ adsorption on the electrode surface (according to the Langmuir adsorption model), to the point where the surface becomes saturated and higher O₂ pressure does not further enhance the cell performance [27]. As the discharge reactions take place in solution at the electrolyte–electrode interface, both oxygen and lithium ions can be mass-transport-limiting. A combination of sufficiently high Li⁺ concentration and elevated oxygen pressure, can help to reduce mass transport limitations [22].

For the given system, a cation concentration of 0.5 M Li⁺ in combination with 4 atm O₂ pressure is sufficient to not be limiting at a current density of $150 \mu\text{A}/\text{cm}^2$. An even higher oxygen pressure could potentially be more beneficial at higher current densities again [29]. From the investigations it is

clear that for GNS electrodes and a current density of $150 \mu\text{A}/\text{cm}^2$, an O_2 pressure above atmosphere level is necessary to facilitate the discharge reactions.

The O_2 pressure will have detrimental impact especially on Li–air batteries that operate at ambient O_2 pressure (0.21 atm). From a technological point of view, this makes battery cell or pack designs with on-board O_2 storage more desirable than open systems. Increasing pressure beyond 4 atm does not seem useful to further boost the discharge capacity of the lithium oxygen cells, but it could be a step towards closed cell systems, in which the amount of oxygen that is necessary to convert a desired amount of lithium into Li_2O_2 is stored inside the cell. This would remove the need for an external oxygen supply and thus reduce the weight of peripheral battery cell or pack components, which in turn increases the energy density of the battery. However, conversely, if high O_2 pressure is beneficial for the discharge process, it may have adverse effects while charging the battery. To our knowledge, there have been no reports that actively varied oxygen pressure to assist the $\text{Li}-\text{O}_2$ cell reactions. Furthermore, a systematic study that relates discharge products size and oxygen pressure remains due.

3.3. Electrolyte Salt

Even in the context of the design of high-capacity electrodes, the electrolyte salt plays a major role, because it strongly interferes with the discharge behavior of the $\text{Li}-\text{O}_2$ battery. Considering that Li^+ and O_2 transport can also be possible limitations, the electrode interface must not only be considered from the cathode perspective, but from the electrolyte side as well. The electrolyte salt, or more specifically, the anion, can easily be exchanged to manipulate the discharge process. For the two TEGDME-based solutions used in this work, the cation concentrations are set to 0.5 M for LiNO_3 and 1.0 M for LiTFSI, which is in accordance with most literature reports. A recent study on the salt anions suggests that the beneficial (capacity-enhancing) effects of LiNO_3 disappear for concentrations of 0.75 M or higher, mainly due to the passivation of the carbon electrode [6]. Note that this cathode-focused study is not meant for direct comparison of the salt anion effects, but rather looks at the electrolyte salt as a parameter to tune the cell performance. Its tremendous effect on the discharge behavior of GNS-foam electrodes is seen in Figure 4, which shows the discharge capacity and the morphology of discharge products as obtained in experiments using LiNO_3 or LiTFSI as electrolyte salt.

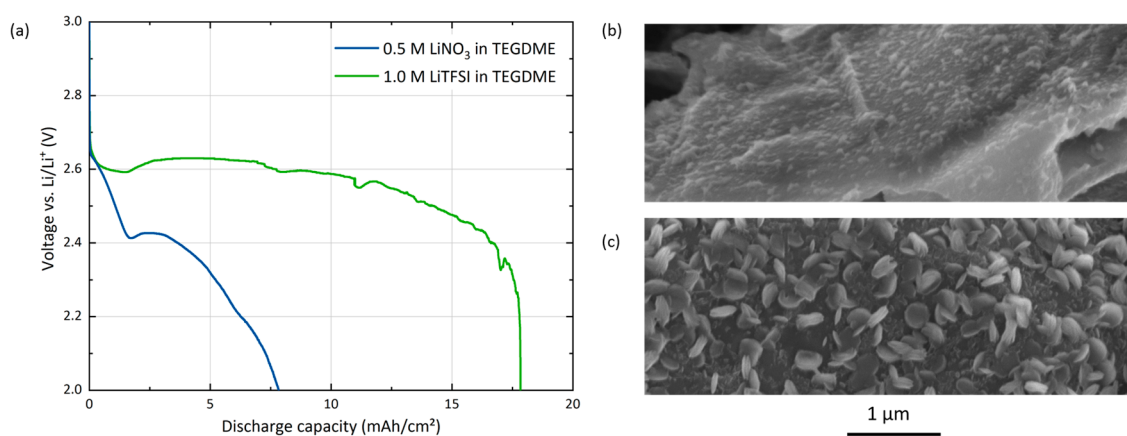


Figure 4. (a) Discharge profiles at $150 \mu\text{A}/\text{cm}^2$ with GNS-foams and $200 \mu\text{L}$ of 0.5 M LiNO_3 or 1.0 M LiTFSI. SEM of characteristic discharge products on GNS for (b) LiTFSI and (c) LiNO_3 .

When directly comparing the discharge performance of both electrolytes, the discharge capacity of GNS-cells more than doubles from $6.9 \text{ mAh}/\text{cm}^2$ for 0.5 M LiNO_3 to $17.8 \text{ mAh}/\text{cm}^2$ for 1.0 M LiTFSI. The LiTFSI cell does not display the expected pronounced two-step discharge profile. At about $2 \text{ mAh}/\text{cm}^2$, there is a minor voltage dip. Then the voltage enters a plateau around 2.55 V, which is followed by a sudden death at the end of discharge. SEM images (b, c) from the electrode top (close to

the O₂ supply) show the expected layer growth of discharge products for LiTFSI in comparison to discharge product particles obtained via LiNO₃. However, this observation does not explain or support the capacity advantage of LiTFSI cells, because discharge product thin films should produce less discharge product per cathode surface area than rotund particles. According to similar experimental studies performed on different electrodes, bigger deposits of discharge products and therefore higher capacities are expected when using LiNO₃ (by enabling the solution-based discharge mechanism) [5–7]. Nonetheless, a majority of publications that reported outstanding capacities used LiTFSI as electrolyte salt [10,14–17,34–36]. To investigate the reasons behind the measured capacity differences, samples of both electrolyte solutions are analyzed:

First, the water contents of both used electrolytes are determined by Karl Fischer titration for LiTFSI-TEGDME (25 ppm) and LiNO₃-TEGDME (164 ppm). Pure TEGDME contained only 12 ppm H₂O. Besides the reactions with the lithium anode, trace amounts of water support the growth of particulate Li₂O₂ and can therefore increase the discharge capacity [4,37–39]. In our experiments, no discolorations (black, grey or white) of the lithium discs were observed after the discharge duration of several days, which indicates that there is negligible water intrusion into the cell setup. The water introduced via LiNO₃, probably as residual water of crystallization, likely supports the formation of the discharge product particles. Since the LiTFSI-electrolyte is practically dry, possible water contamination is not a reasonable explanation for the superior discharge performance.

Second, the conductivity of both electrolytes is measured to be 2.14 mS/cm for 1.0 M LiTFSI and 0.16 mS/cm for 0.5 M LiNO₃ in TEGDME. The ratio of the conductivities matches literature data using similar electrolyte solutions [7]. This is further supported by cyclic voltammetry (CV) experiments (Figure S3), in which the LiTFSI-based electrode shows a much larger peak current than LiNO₃. If the Li⁺ transport is the current-density-limiting factor (when using thick electrodes), then LiTFSI-based electrolytes have a clear advantage due to their high ionic conductivity [5,7].

A more detailed analysis of discharged electrodes on the microscale is carried out in the electron microscope with EDS. Figure 5 shows SEM images from the bottom and the top of a GNS electrode discharged with LiTFSI.

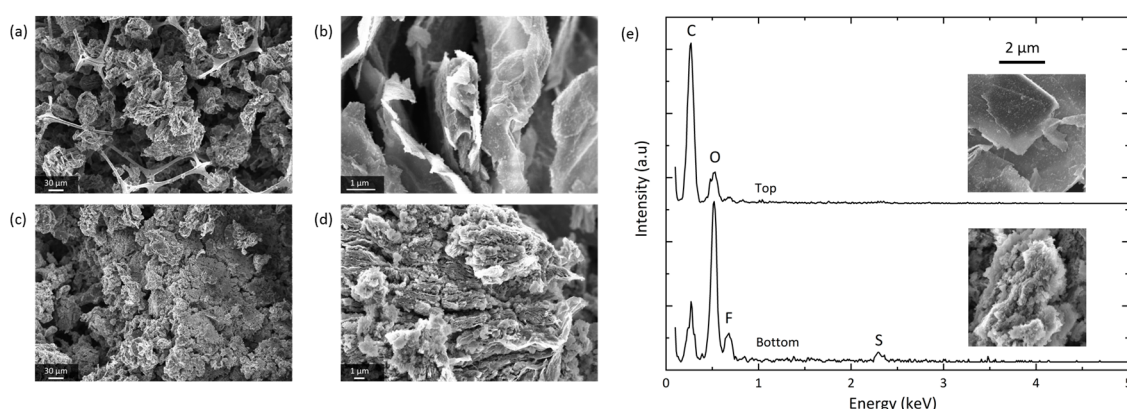


Figure 5. SEM images of a GNS-foam electrode after discharge to 17.8 mAh/cm² at 150 μ A/cm² with 200 μ L of 1.0 M LiTFSI-TEGDME. (a) Overview image of electrode top. (b) Intact, but only thin film-coated GNS at the electrode top. (c) Expansion of a GNS bundle at the electrode bottom. (d) Heavily deteriorated GNS at the electrode bottom. (e) EDS spot spectra of GNS at electrode top and bottom with corresponding SEM images.

The visible discharge products are not similar in shape to the regularly shaped particles that are obtained with the LiNO₃ electrolyte. Instead, there are either subtle thin films or decomposed GNS particles with highly irregular shapes. Thin film coatings and intact GNS are found at the electrode top (Figure 5a,b), whereas strongly deteriorated areas make up a major part of the electrode bottom (separator side, Figure 5c,d). The distribution of degraded GNS is therefore similar to LiNO₃

cells, where damage is mainly observed on the lithium-rich side of the electrode that is facing the separator [18]. The amount of exfoliated GNS can hardly be quantified, but considering the large discharge capacity, it is expected that there is a larger share of exfoliated GNS in LiTFSI cells than in LiNO₃ cells.

Considering the known instability of the electrode–electrolyte interface and reactive oxygen species that are formed during discharge, it should be kept in mind that Li–F (and also Li–S and Li–N) chemistry may compete with the desired Li–O₂ reactions. EDS spot measurements on GNS from the bottom and top of a discharge electrode (Figure 5e), show fluorine and sulfur signatures in addition to the expected carbon and oxygen signals, even though all samples were washed thoroughly with DME. Decomposition products of LiTFSI could have been incorporated into the discharge product layer. Not containing any fluorine (provided that no fluorine-containing binders or solvents are used) is a clear benefit of LiNO₃-based cells.

For GNS electrodes, there is a possibility that the LiTFSI cells draw most of their capacity from the stage II discharge mechanism. The combination of graphite, as a layered material and a well-known intercalation host, and LiTFSI, as a promotor of thin film discharge products, may facilitate the carbon expansion and exfoliation process at even higher discharge voltages. A key property of the LiTFSI electrolyte, which could promote this behavior, is its high degree of ionic dissociation, which enables Li⁺ to intercalate into the graphite layers and allows for reactions in-between them [22,40]. In that case, the combination of GNS and LiTFSI turns out to be a highly synergistic combination in which properties like the ionic conductivity outweigh the benefits of alternative discharge pathways. The bias between the discharge model and the achieved discharge capacities with LiNO₃/LiTFSI should be investigated in a systematic study, in which rate capability tests (and also cyclability tests) are carried out for both electrolytes in direct comparison.

3.4. Capacity Optimization

The previous sections demonstrated the impact of three cell parameters on the discharge capacity of GNS electrodes. There is another, although rather more technical parameter that needs to be optimized in order to increase the capacity: the electrolyte volume. By employing 200 μL of electrolyte, the electrode has not been fully utilized as tradeoff for more consistent discharge capacities and reasonable test times. Going up to the maximum filling (400 μL) allows us to linearly scale up the capacities to 13.0 mAh/cm² for LiNO₃ and 47.5 mAh/cm² for LiTFSI (see Figure S4). Improving the cathode utilization allows us to get closer to the upper limit of the lithium anode conversion, which is the main challenge for high-capacity Li–O₂ batteries. We emphasize that it is important to always report the amount of electrolyte used, because it can account for a large share of the overall weight of the cell stack. Without detailed electrode and electrolyte data, the energy content of a Li–O₂ cell cannot be assessed on the stack or cell level.

Now, the discussed cell parameters are brought together and combined with a scaled-up electrode. So far, all batteries featured in this work have been limited by processes that are related to cathode–electrolyte interface. Aiming for full conversion of the lithium anode (40 mg, equal to 154.4 mAh or 60.7 mAh/cm²), a cell is assembled using three stacked GNS-loaded foam electrodes and it is discharged at 150 μA/cm² at high O₂ pressure of 11 atm with the 1.0 M LiTFSI electrolyte. In this cell, the total cathode mass (40.9 mg) and electrolyte volume (1.2 mL) are deliberately oversized to get close to the lithium limit. While the beneficial effects of increased O₂ pressure on capacity are reached when applying about 4 atm, this experiment was run at the limit provided by the cell hardware. The current density is not decreased in order to keep the test time reasonably short. The discharge profile is shown in Figure 6.

The stacking of GNS-foam cathodes proves to be an effective strategy to produce large amounts of discharge products and generate an outstanding discharge capacity. After several hours of discharge operation, at around 2.8 mAh/cm², the battery shows a pronounced voltage drop to 2.44 V, which likely marks the onset of stage II discharge and the beginning of GNS exfoliation. The discharge of this

cell ends with a sudden death after a capacity of 56.3 mAh/cm^2 (143.1 mAh). This equals 93% of the theoretical capacity of the lithium anode. Referred to as the GNS weight of 24.4 mg , this means a carbon-specific capacity of $5860 \text{ mAh/g}_{\text{carbon}}$. The corresponding mass of deposited Li_2O_2 is five times higher than the mass of the GNS as active material.

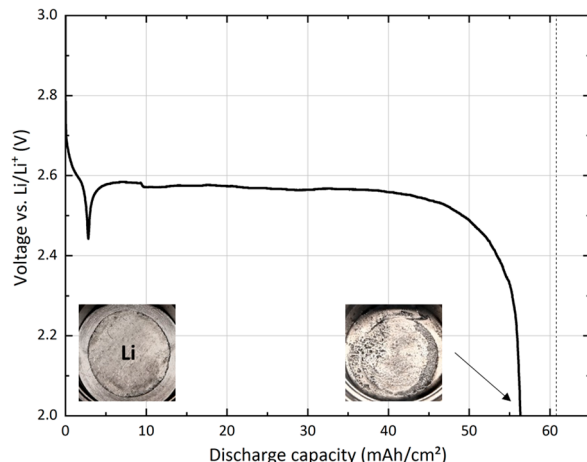


Figure 6. Discharge profile of a scaled-up cell using a stack of three GNS-loaded foam electrodes. The pictures in the graph depict the lithium anode before and after full discharge. The dashed vertical line marks the upper limit for the full consumption of the anode.

The discharge products of this cell are analyzed post mortem and Figure 7 shows the resulting XRD diffractogram and the Raman spectrum of the bottom electrode (closest to the separator).

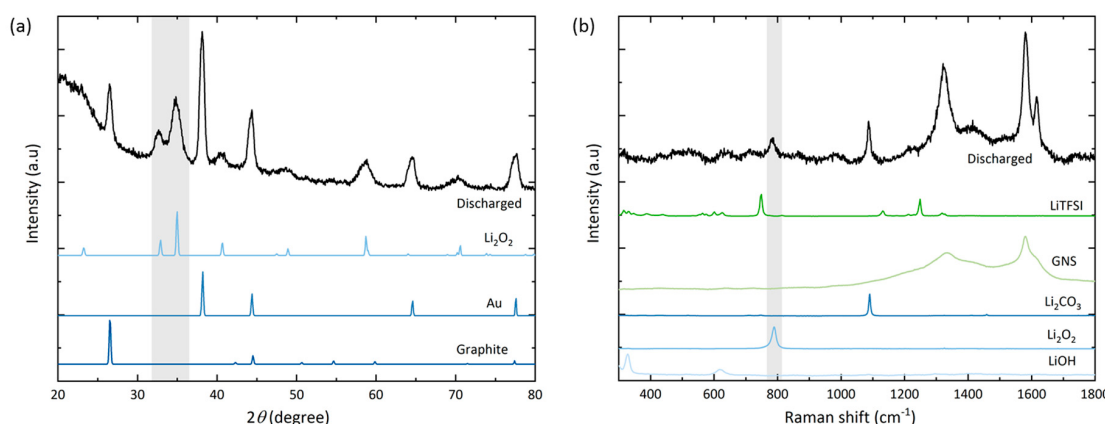


Figure 7. (a) XRD diffractogram and (b) Raman spectrum of the discharged (bottom) electrode. The highlighted grey area marks the Raman band and reflexes of Li_2O_2 , respectively.

Qualitative post mortem analysis indicates the occurrence of undesired side reactions: XRD (Figure 7a) confirms the formation of mainly Li_2O_2 , but the diffractogram does not show any side reaction products such as (crystalline) Li_2CO_3 . However, Raman spectroscopy that was carried out on the electrode bottom (Figure 7b) captures more signal intensity for Li_2CO_3 than Li_2O_2 . This is in agreement with prior observations from a fully discharged GNS electrode with the LiNO_3 -electrolyte [18]. A noticeable feature in the Raman spectrum of the discharged GNS electrode is a higher carbon peak intensity ratio (I_D/I_G , with the graphic G-band at 1582 cm^{-1} and the defect-related D-band at 1350 cm^{-1}), which may be caused by the narrowing and decrease in G-band signal due to a loss of graphite crystallinity [41]. Another observation is the appearance of a signal at 1615 cm^{-1} , which could be a shifted D'-band (1620 cm^{-1}) or a split G-band (1608 cm^{-1}), which may be related to intercalation or carbon decomposition processes [42].

The exact role of Li^+ intercalation during the second stage of discharge, remains unclear. It could be elucidated by operando XRD and Raman spectroscopy. SEM images (Figure S5) were taken at the top, middle and bottom foam discs, respectively. Notably, the bottom side of the electrode closest to the lithium anode shows the most structurally damaged GNS and irregularly shaped discharge products, similar to the SEM images in Figure 5. Looking at the overall level of GNS decomposition, only a small share of GNS has undergone deterioration in order to reach this high capacity.

In this experiment, the discharge is limited by the availability of lithium, which has been almost fully removed from the cell bottom. Even close to the end of discharge, this battery stably operates at 2.55 V, and its state of discharge still leaves room for further discharge product deposition. In cathode-limited cells, the discharge will stop, once all electrochemically active GNS is passivated, which is also linked to the state of decomposition of GNS. We estimate that a single GNS-foam electrode is suitable for the conversion of approximately 15 mg of lithium. Using a recently proposed performance metric, which takes both the electrode mass and the discharge products mass into account [12], the specific capacity is 876 mAh/g(electrode + Li_2O_2). This is about 75% of the theoretical capacity of pure Li_2O_2 , which is used to calculate the theoretical specific energy of $\text{Li}-\text{O}_2$ batteries. Note that this estimation assumes that there is only Li_2O_2 ($M = 45.88 \text{ g/mol}$) formed as discharge product and no side reactions occur. The energy released by the discharge of this battery equates to 364 mWh and the cell has a total mass of 1.65 g. On the level of the cell, the specific energy is 225 Wh/kg. Due to the significant electrolyte mass, which is necessary to increase the cathode utilization, the specific energy is far from the desired theoretical levels and closer to Li-ion batteries.

This study points out the dilemma of air electrode design: most cathodes reported in literature, especially those with (carbon) mass loadings $<0.1 \text{ mg}$, are greatly undersized and unsuited to convert practically relevant amounts of lithium. If highly porous electrodes are scaled up to host the desired amount of discharge products at a given current density, then this architecture requires a large amount of electrolyte to be fully utilized. This in return counteracts the benefits of the lightweight design. The goal of $\text{Li}-\text{O}_2$ batteries with specific energies larger than 500 Wh/kg can only be reached with air electrodes that reach the maximum capacity with the minimum amount both of mass and volume. Besides the correct dimensioning of the electrodes, the cell reactions require further understanding to develop strategies that can prevent side reactions, intrinsic passivation and large microstructural volume changes. The system presented here can surely serve as an effective low-power primary battery, but it has to be questioned whether this can be recharged or cycled hundreds of times at a maximum depth of discharge. Once dissolved, the lithium anode will be hard to restore without loss of electrochemically active material in an O_2 -rich environment. Considering the condition of the lithium, separate electrode compartments and anode protection measures are advisable [43].

4. Conclusions

In summary, GNS-loaded foams prove to be air electrodes capable of reaching high areal capacities up to 56.3 mAh/cm^2 when discharged under suitable conditions: (i) an appropriate current density ($150 \mu\text{A}/\text{cm}^2$ or lower), (ii) an O_2 pressure of 4 atm or higher, (iii) LiTFSI as electrolyte salt and (iv) scaled-up cathodes filled with a sufficient amount of electrolyte. If the target application of the battery allows it, the discharge current density should be minimal for maximum discharge capacity and voltage. The oxygen pressure must be sufficiently high to prevent kinetic penalties, and increasing it further may result in a decent capacity boost for many cathode designs reported in literature. Contrary to expectations, replacing LiNO_3 as electrolyte salt with LiTFSI significantly boosts discharge capacity, likely due to its improved Li^+ transport properties and synergistic effects together with GNS. We conclude that LiNO_3 is the more suitable salt for fundamental studies, while LiTFSI is the better choice in terms of discharge performance. An appropriate amount of electrolyte is vital to increase the degree of cathode utilization and is well worth investigating in detail.

Lastly, we want to emphasize that optimized combinations of the aforementioned operation parameters are easy to implement and this may significantly enhance the discharge capabilities of air

electrodes. Future challenges will also need to address the fundamental tradeoffs between energy, power, capacity, and electrode mass and volume. Therefore, if Li-O₂ batteries are to make it into practical application, a balance must be found.

Supplementary Materials: The following are available online at <http://www.mdpi.com/2313-0105/6/3/36/s1>, Additional electrochemical data and SEM images. Figure S1: (a) Logarithmic representation and (b) normalized discharge profiles of GNS-foam electrodes with current densities between 15 μA/cm² and 1.5 mA/cm², Figure S2: Discharge profile of a GNS-foam electrode at 150 μA/cm² and an oxygen pressure of 11 atm, Figure S3: Cyclic voltammetry $j(U)$ profile for Li-O₂ cells with GNS-foam electrodes in combination with 200 μL of either 1.0 M LiTFSI or 0.5 M LiNO₃ in TEGDME as electrolyte. The CV measurements are carried out with a Zahner IM6 potentiostat. The sweep rate is 100 μV/s and tests start with a negative sweep from the equilibrium potential of the cell (\approx 3 V), Figure S4: Effects of the electrolyte volume (100–400 μL) on the discharge capacity of GNS-foam electrodes, Figure S5: Three GNS-foam electrodes were stacked in a single cell and discharged to 56.2 mAh/cm². The figure shows the SEM images of GNS from the top (a), middle (b) and bottom (c) electrode.

Author Contributions: P.W.: conceptualization, investigation methodology, writing—original draft. J.K.: writing, methodology—original draft. U.S.: supervision, writing—review and editing. All authors have read and agreed to the published version of the manuscript.

Funding: This research was financially supported by the research training group 1856 “Integrated Energy Supply Modules for Roadbound E-Mobility” (mobilEM), funded by the German Research Foundation (DFG), and the Bosch Research Foundation.

Conflicts of Interest: The authors declare no conflict of interest.

References

1. Cano, Z.P.; Banham, D.; Ye, S.; Hintennach, A.; Lu, J.; Fowler, M.; Chen, Z. Batteries and fuel cells for emerging electric vehicle markets. *Nat. Energy* **2018**, *3*, 279–289. [[CrossRef](#)]
2. Xia, C.; Kwok, C.Y.; Nazar, L.F. A high-energy-density lithium-oxygen battery based on a reversible four-electron conversion to lithium oxide. *Science* **2018**, *361*, 777–781. [[CrossRef](#)] [[PubMed](#)]
3. Huang, J.; Peng, Z. Understanding the reaction interface in lithium-oxygen batteries. *Batter. Supercaps* **2019**, *2*, 37–48. [[CrossRef](#)]
4. Aetukuri, N.B.; McCloskey, B.D.; García, J.M.; Krupp, L.E.; Viswanathan, V.; Luntz, A.C. Solvating additives drive solution-mediated electrochemistry and enhance toroid growth in non-aqueous Li-O₂ batteries. *Nat. Chem.* **2015**, *7*, 50–56. [[CrossRef](#)]
5. Burke, C.M.; Pande, V.; Khetan, A.; Viswanathan, V.; McCloskey, B.D. Enhancing electrochemical intermediate solvation through electrolyte anion selection to increase nonaqueous Li-O₂ battery capacity. *Proc. Natl. Acad. Sci. USA* **2015**, *112*, 9293–9298. [[CrossRef](#)] [[PubMed](#)]
6. Iliksu, M.; Khetan, A.; Yang, S.; Simon, U.; Pitsch, H.; Sauer, D.U. Elucidation and comparison of the effect of LiTFSI and LiNO₃ salts on discharge chemistry in nonaqueous Li-O₂ batteries. *ACS Appl. Mater. Interfaces* **2017**, *9*, 19319–19325. [[CrossRef](#)] [[PubMed](#)]
7. Sharon, D.; Hirsberg, D.; Salama, M.; Afri, M.; Frimer, A.A.; Noked, M.; Kwak, W.-J.; Sun, Y.-K.; Aurbach, D. The mechanistic role of Li⁺ dissociation level in aprotic Li-O₂ battery. *ACS Appl. Mater. Interfaces* **2016**, *8*, 5300–5307. [[CrossRef](#)]
8. Christensen, J.; Albertus, P.; Sanchez-Carrera, R.S.; Lohmann, T.; Kozinsky, B.; Liedtke, R.; Ahmed, J.; Kojic, A. A critical review of Li/Air batteries. *J. Electrochem. Soc.* **2012**, *159*, R1–R30. [[CrossRef](#)]
9. Grande, L.; Paillard, E.; Hassoun, J.; Park, J.-B.; Lee, Y.-J.; Sun, Y.-K.; Passerini, S.; Scrosati, B. The lithium/air battery: Still an emerging system or a practical reality? *Adv. Mater.* **2015**, *27*, 784–800. [[CrossRef](#)] [[PubMed](#)]
10. Balaish, M.; Jung, J.-W.; Kim, I.-D.; Ein-Eli, Y. A critical review on functionalization of air-cathodes for nonaqueous Li-O₂ batteries. *Adv. Funct. Mater.* **2019**. [[CrossRef](#)]
11. Yang, S.; He, P.; Zhou, H. Research progresses on materials and electrode design towards key challenges of Li-Air batteries. *Energy Storage Mater.* **2018**, *13*, 29–48. [[CrossRef](#)]
12. Kwak, W.-J.; Rosy; Sharon, D.; Xia, C.; Kim, H.; Johnson, L.R.; Bruce, P.G.; Nazar, L.F.; Sun, Y.-K.; Frimer, A.A.; et al. Lithium-oxygen batteries and related systems: Potential, status, and future. *Chem. Rev.* **2020**. [[CrossRef](#)] [[PubMed](#)]
13. Noked, M.; Schroeder, M.A.; Pearse, A.J.; Rubloff, G.W.; Lee, S.B. Protocols for evaluating and reporting Li-O₂ cell performance. *J. Phys. Chem. Lett.* **2016**, *7*, 211–215. [[CrossRef](#)]

14. Nomura, A.; Ito, K.; Kubo, Y. CNT sheet air electrode for the development of ultra-high cell capacity in lithium-air batteries. *Sci. Rep.* **2017**, *7*, 45596. [[CrossRef](#)]
15. Lin, Y.; Moitiso, B.; Martinez-Martinez, C.; Walsh, E.D.; Lacey, S.D.; Kim, J.-W.; Dai, L.; Hu, L.; Connell, J.W. Ultrahigh-capacity lithium-oxygen batteries enabled by dry-pressed holey graphene air cathodes. *Nano Lett.* **2017**, *17*, 3252–3260. [[CrossRef](#)] [[PubMed](#)]
16. Tan, P.; Shyy, W.; An, L.; Wei, Z.H.; Zhao, T.S. A gradient porous cathode for non-aqueous lithium-air batteries leading to a high capacity. *Electrochim. Commun.* **2014**, *46*, 111–114. [[CrossRef](#)]
17. Lee, Y.; Park, S.H.; Kim, S.H.; Ko, Y.; Kang, K.; Lee, Y.J. High-rate and high-areal-capacity air cathodes with enhanced cycle life based on RuO₂-MnO₂ bifunctional electrocatalysts supported on CNT for pragmatic Li-O₂ batteries. *ACS Catal.* **2018**, *8*, 2923–2934. [[CrossRef](#)]
18. Wunderlich, P.; Küpper, J.; Simon, U. Anomalous discharge behavior of graphite nanosheet electrodes in lithium-oxygen batteries. *Materials* **2019**, *13*, 43. [[CrossRef](#)]
19. Lu, Y.-C.; Shao-Horn, Y. Probing the reaction kinetics of the charge reactions of nonaqueous Li-O₂ batteries. *J. Phys. Chem. Lett.* **2013**, *4*, 93–99. [[CrossRef](#)]
20. Lau, S.; Archer, L.A. Nucleation and growth of lithium peroxide in the Li-O₂ battery. *Nano Lett.* **2015**, *9*, 5995–6002. [[CrossRef](#)]
21. Gallant, B.M.; Kwabi, D.G.; Mitchell, R.R.; Zhou, J.; Thompson, C.V.; Shao-Horn, Y. Influence of Li₂O₂ morphology on oxygen reduction and evolution kinetics in Li-O₂ batteries. *Energy Environ. Sci.* **2013**, *6*, 2518–2528. [[CrossRef](#)]
22. Gittleson, F.S.; Jones, R.E.; Ward, D.K.; Foster, M.E. Oxygen solubility and transport in Li-air battery electrolytes: Establishing criteria and strategies for electrolyte design. *Energy Environ. Sci.* **2017**, *10*, 1167–1179. [[CrossRef](#)]
23. Yin, Y.; Torayev, A.; Gaya, C.; Mammeri, Y.; Franco, A.A. Linking the performances of Li-O₂ batteries to discharge rate and electrode and electrolyte properties through the nucleation mechanism of Li₂O₂. *J. Phys. Chem. C* **2017**, *121*, 19577–19585. [[CrossRef](#)]
24. Griffith, L.D.; Sleighholme, A.; Mansfield, J.F.; Siegel, D.J.; Monroe, C.W. Correlating Li/O₂ cell capacity and product morphology with discharge current. *ACS Appl. Mater. Interfaces* **2015**, *7*, 7670–7678. [[CrossRef](#)] [[PubMed](#)]
25. Torayev, A.; Rucci, J.A.; Magusin, P.M.; Demortiere, A.; De Andrade, V.; Grey, C.P.; Merlet, C.; Franco, A.A. Stochasticity of pores interconnectivity in Li-O₂ batteries and its impact on the variations in electrochemical performance. *J. Phys. Chem. Lett.* **2018**, *9*, 791–797. [[CrossRef](#)] [[PubMed](#)]
26. Cui, Z.H.; Guo, X.X.; Li, H. Equilibrium voltage and overpotential variation of nonaqueous Li-O₂ batteries using the galvanostatic intermittent titration technique. *Energy Environ. Sci.* **2015**, *8*, 182–187. [[CrossRef](#)]
27. Viswanathan, V.; Nørskov, J.; Speidel, A.; Scheffler, R.; Gowda, S.; Luntz, A. Li-O₂ kinetic overpotentials: Tafel plots from experiment and first-principles theory. *J. Phys. Chem. Lett.* **2013**, *4*, 556–560. [[CrossRef](#)]
28. McCloskey, B.D.; Speidel, A.; Scheffler, R.; Miller, D.C.; Viswanathan, V.; Hummelshøj, J.S.; Nørskov, J.K.; Luntz, A.C. Twin problems of interfacial carbonate formation in nonaqueous Li-O₂ batteries. *J. Phys. Chem. Lett.* **2012**, *3*, 997–1001. [[CrossRef](#)]
29. Nemanick, E.J.; Hickey, R.P. The effects of O₂ pressure on Li-O₂ secondary battery discharge capacity and rate capability. *J. Power Sources* **2014**, *252*, 248–251. [[CrossRef](#)]
30. Yang, X.-H.; Xia, Y.-Y. The effect of oxygen pressures on the electrochemical profile of lithium/oxygen battery. *J. Solid State Electrochem.* **2010**, *14*, 109–114. [[CrossRef](#)]
31. McCloskey, B.D.; Scheffler, R.; Speidel, A.; Girishkumar, G.; Luntz, A.C. On the mechanism of nonaqueous Li-O₂ electrochemistry on C and its kinetic overpotentials: Some implications for Li-Air batteries. *J. Phys. Chem. C* **2012**, *116*, 23897–23905. [[CrossRef](#)]
32. Read, J.; Mutolo, K.; Ervin, M.; Behl, W.; Wolfenstine, J.; Driedger, A.; Foster, D. Oxygen transport properties of organic electrolytes and performance of lithium-oxygen battery. *J. Electrochem. Soc.* **2003**, *150*, A1351. [[CrossRef](#)]
33. Li, J.; Gao, M.; Tong, S.; Luo, C.; Zhu, H.; Taketsugu, T.; Uosaki, K.; Wu, M. Effect of O₂ adsorption on the termination of Li-O₂ batteries discharge. *Electrochim. Acta* **2020**, *340*, 135977. [[CrossRef](#)]
34. Lacey, S.D.; Kirsch, D.J.; Li, Y.; Morgenstern, J.T.; Zarket, B.C.; Yao, Y.; Dai, J.; Garcia, L.Q.; Liu, B.; Gao, T.; et al. Extrusion-based 3D printing of hierarchically porous advanced battery electrodes. *Adv. Mater.* **2018**, *30*, 1705651. [[CrossRef](#)] [[PubMed](#)]

35. Zhao, G.; Zhang, L.; Lv, J.; Li, C.; Sun, K. Vertically aligned graphitic carbon nanosheet arrays fabricated from graphene oxides for supercapacitors and Li-O₂ batteries. *Chem. Commun.* **2016**, *52*, 6403–6406. [[CrossRef](#)]
36. Yoo, E.; Zhou, H. Carbon cathodes in rechargeable lithium-oxygen batteries based on double-lithium-salt electrolytes. *ChemSusChem* **2016**, *9*, 1249–1254. [[CrossRef](#)]
37. Schwenke, K.U.; Metzger, M.; Restle, T.; Piana, M.; Gasteiger, H.A. The influence of water and protons on Li₂O₂ crystal growth in aprotic Li-O₂ cells. *J. Electrochem. Soc.* **2015**, *162*, A573–A584. [[CrossRef](#)]
38. Kwabi, D.G.; Batcho, T.P.; Feng, S.; Giordano, L.; Thompson, C.V.; Shao-Horn, Y. The effect of water on discharge product growth and chemistry in Li-O₂ batteries. *Phys. Chem. Chem. Phys.* **2016**, *18*, 24944–24953. [[CrossRef](#)]
39. Dai, A.; Li, Q.; Liu, T.; Amine, K.; Lu, J. Fundamental understanding of water-induced mechanisms in Li-O₂ batteries: Recent developments and perspectives. *Adv. Mater.* **2018**, *31*, e1805602. [[CrossRef](#)]
40. Chung, G.C.; Kim, H.J.; Yu, S.I.; Jun, S.H.; Choi, J.W.; Kim, M.H. Origin of graphite exfoliation an investigation of the important role of solvent cointercalation. *J. Electrochem. Soc.* **2000**, *147*, 4391–4398. [[CrossRef](#)]
41. Jorio, A.; Ferreira, E.H.M.; Moutinho, M.V.O.; Stavale, F.; Achete, C.A.; Capaz, R.B. Measuring disorder in graphene with the G and D bands. *Phys. Status Solidi* **2010**, *247*, 2980–2982. [[CrossRef](#)]
42. Sole, C.; Drewett, N.E.; Hardwick, L.J. In situ Raman study of lithium-ion intercalation into microcrystalline graphite. *Faraday Discuss.* **2014**, *172*, 223–237. [[CrossRef](#)] [[PubMed](#)]
43. Bi, X.; Amine, K.; Lu, J. The importance of anode protection towards lithium oxygen batteries. *J. Mater. Chem. A* **2020**, *8*, 3563–3573. [[CrossRef](#)]



© 2020 by the authors. Licensee MDPI, Basel, Switzerland. This article is an open access article distributed under the terms and conditions of the Creative Commons Attribution (CC BY) license (<http://creativecommons.org/licenses/by/4.0/>).